

# Parylene-Based Electrochemical-MEMS Force Sensor for Studies of Intracortical Probe Insertion Mechanics

Brian J. Kim, Christian A. Gutierrez, and Ellis Meng, *Senior Member, IEEE*

**Abstract**—To investigate the mechanical interactions between the implanted cortical multielectrode probes and brain tissue, a Parylene C-based electrochemical-microelectromechanical systems force sensor array was developed. The array consists of seven linearly distributed sensor units arranged along the length of a flexible Parylene C microchannel. The seven sensor units are formed by eight fluidically coupled and adjacent platinum electrode pairs enclosed within the microchannel. Deformation of the top surface of the mechanically compliant microchannel changes the volumetric conduction path between the pairs of sensing electrodes, and therefore, the measured electrochemical impedance, which is proportional to the magnitude of the contacting force. Each sensor unit demonstrated a linear response from 0 to 60 mN with a sensitivity of  $0.13 \pm 0.01$  percentage change in impedance/ $\mu\text{N}$  ( $\%/ \mu\text{N}$ ; mean  $\pm$  SE,  $n = 6$ ). The sensor arrays were mounted onto a ceramic intracortical probe and inserted into the tissue phantoms to verify *in situ* functionality and assess interfacial probe mechanics. Probe surface force distribution was measured under various insertion speeds and the results indicated that interfacial forces are distributed nonuniformly along the probe shaft length, concentrating within the first 1 mm of the advancing probe tip. Faster insertion speeds were also found to decrease the magnitude of the interfacial forces, suggesting that the tissue strain during cortical implantation may be minimized through appropriate selection of the insertion speed. [2014-0320]

**Index Terms**—Force sensor, electrochemical-microelectromechanical systems (EC-MEMS), electrochemical sensing, electrochemical transduction, impedance-based sensor, liquid impedance, Parylene C, mechanotransduction.

## I. INTRODUCTION

CHRONICALLY implanted intracortical probes provide a means for recording neural signals or applying electrical stimuli within the sensory and/or motor areas of the brain, fueling their development for clinical brain-machine interfaces (BMIs) and neuromodulation. However, the potential of these implantable neural prosthetics

as enabling technologies is challenged by the delicate interfacial mechanics between the probe and the soft cortical tissue it penetrates [1]. The initial stab wound injury from implantation of rigid metal or silicon probes and the resultant disruptions of the blood-brain-barrier (BBB), combined with the resulting foreign body response have been found to diminish their efficacy for chronic recordings [2]. In addition, cortical micromotion due to vascular pulsing induces a constant mechanical agitation between the soft tissue and rigid probes [3]. The corresponding effects on chronic probe performance have yet to be fully understood, largely due to inadequate measurement technology.

Previously, external load cells were used to measure macroscale normal insertion forces [4]–[6] as well as to compare differing probe tip designs [4], [7], but out-of-plane stresses acting on the probe surface could not be detected, providing limited insight into interfacial phenomena. Also, studies comparing normal insertion force measurements alone have found poor correlation between normal force magnitudes and chronic probe performance [7]. Modeling [8]–[10] and *ex vivo* probe implantation experiments utilizing cross-sectional viewing planes [11] have provided great insight into the theoretical distribution of strains and forces during implantation, at the probe-tissue interface, and during micromotion events. However, quantitative data obtained from surgical and *in vivo* conditions to capture these mechanical interactions during insertion and micromotion events in real time is lacking.

Technologies to integrate sensors on probes have already been developed, but many of these sensors are difficult to apply or integrate and provide limited access to interfacial mechanics. For example, CMOS sensors integrated on a silicon probe were used to measure effects of insertion-derived probe deflection stresses during implantation [12]. Though resultant probe deflection due to insertion into tissue does capture some interfacial forces, the method cannot detect interfacial forces normal to the probe from the surrounding neural tissue. Also, these sensors are currently limited to silicon probes. Furthermore, commercial probes readily available to neuroscience researchers do not offer the option of sensor integration. A more versatile approach is necessary to enable comparative studies between different electrode designs and materials. Sensors must be able to: accommodate small shank areas, integrate with CMOS-incompatible electrode shank materials, and operate in aqueous and saline environments. By utilizing sensor technology in addition to histological

Manuscript received October 15, 2014; revised January 8, 2015; accepted April 1, 2015. Date of publication April 16, 2015; date of current version September 29, 2015. This work was supported in part by the Engineering Research Centers Program through the National Science Foundation under Award EEC-0310723, in part by the University of Southern California Provost Ph.D. Fellowship, and in part by the Bill and Melinda Gates Foundation. Subject Editor A. J. Ricco.

B. J. Kim is with the Department of Biomedical Engineering, University of Southern California, Los Angeles, CA 90089 USA (e-mail: brianjk@usc.edu).

C. A. Gutierrez is with Fluid Synchrony, LLC, Los Angeles, CA 90089 USA (e-mail: christian@fluidsynchrony.com).

E. Meng is with the Department of Biomedical Engineering, Ming Hsieh Department of Electrical Engineering, University of Southern California, Los Angeles, CA 90089 USA (e-mail: ellis.meng@usc.edu).

Color versions of one or more of the figures in this paper are available online at <http://ieeexplore.ieee.org>.

Digital Object Identifier 10.1109/JMEMS.2015.2420043

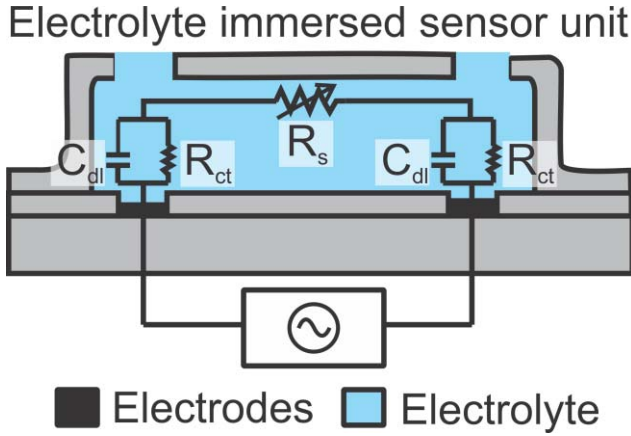


Fig. 1. Equivalent circuit model of measuring the electrochemical impedance between a pair of electrodes in an electrolyte. Note the use of the simplified Randles circuit model at the two electrode-electrolyte interfaces.

methods, benchtop or *in vivo* studies (such as comparing probe designs, materials, and insertion parameters) can be conducted to correlate interfacial mechanical interaction data with chronic neural probe integration and performance. In addition, these integrated devices can be used to effectively characterize micromotion-related forces and their effects on long-term performance. Understanding these design factors and corresponding mechanical interactions at the prosthesis-tissue interface *in vivo* is one large step towards the realization of reliable probe technologies that minimize tissue damage and the related immunological responses that hinder the progress of chronically implanted neural prosthetic technologies [13].

To address this unmet need, we adapted our Parylene C-based electrochemical-MEMS (EC-MEMS) sensing technology [14]–[16] to transduce force and pressure distributions directly on the probe surface. Here, we present a sensor layout capable of integrating directly onto existing implantable ceramic electrode shanks, with its subsequent device packaging and testing, including thermal annealing. We also demonstrate measurement, for the first time, of the normal force distribution produced along the shank surface in agarose tissue phantoms.

## II. OPERATING PRINCIPLE AND DESIGN

EC-MEMS sensors use electrochemical impedance as a sensing modality [14], [17], [18]. These sensors usually consist of a pair of electrodes exposed to an electrolyte (a conductive fluid) enclosed within a Parylene C (hereon referred to as Parylene) microstructure. Integrated port openings allow fluid exchange with the local environment. To understand the impedance-based transduction mechanism, it is useful to consider the well-known simplified Randles circuit model of the electrode-electrolyte interface [19].

A more detailed discussion of the simplified Randles circuit model for EC-MEMS sensors can be found in previous work [14], but is briefly summarized here. In the model, the double-layer capacitance ( $C_{dl}$ ) and the charge transfer resistance ( $R_{ct}$ ) approximate the complex charge transfer phenomena from the electrolyte by the electrodes (Fig. 1).

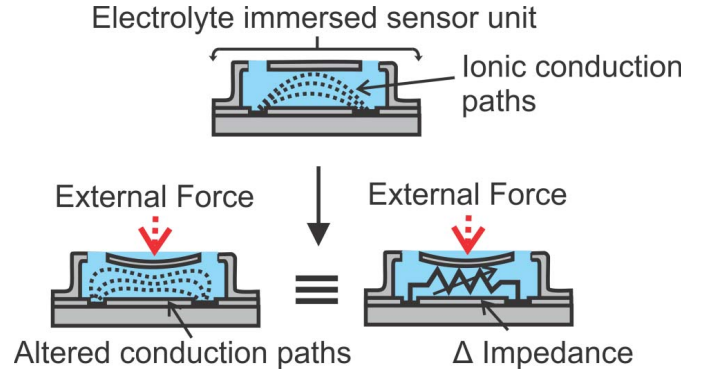


Fig. 2. Schematic of electrochemical impedance-based transduction method of contact forces utilizing a flexible, mechanically compliant microchamber.

At this electrode-electrolyte interface, there exist two layers of charge known as the double-layer, which is formed by corresponding ions and molecules in the electrolyte responding to excess charges on the surface of the electrode [20]. The reversible reactions at this interface are responsible for the capacitive and resistive characteristics observed as charge is transferred between the electrode and electrolyte [21], [22].

An alternating current (AC) signal applied to the EC-MEMS sensors is used to measure the electrochemical impedance between a pair of electrodes in an electrolyte. If the frequency of this AC signal is sufficiently high ( $f_{meas}$ ), the double-layer effects are diminished as the solution resistance ( $R_s$ ) dominates the impedance response (Fig. 1). Thus, in this sensing configuration, the sensor is effectively a variable resistor, and a number of variables (conductive media ( $\rho$ ), distance between the electrodes ( $l$ ), and cross sectional area ( $A$ )) can affect a change in the measured solution resistance, and thus electrochemical impedance, accordingly. The complex impedance for a two-electrode system is expressed in (1) with the high-frequency approximation provided in (2).

$$Z = \frac{\frac{1}{j\omega C_{dl}} R_{ct}}{\frac{1}{j\omega C_{dl}} + R_{ct}} + R_s + \frac{\frac{1}{j\omega C_{dl}} R_{ct}}{\frac{1}{j\omega C_{dl}} + R_{ct}} = \frac{2R_{ct}}{1 + R_{ct}j\omega C_{dl}} + R_s \quad (1)$$

$$Z \approx R_s = \frac{\rho l}{A}; \quad \text{for sufficiently high } \omega \quad (2)$$

The principle of sensor operation relies on external contact forces deforming a compliant electrolyte-filled structure in the normal direction and redistributing the fluid contained within the chamber. This alters the volumetric ionic conduction path of current-carrying ions in the fluid, in effect modifying the cross sectional area between the two electrodes, and registering as a change in the magnitude of the solution impedance (Fig. 2). In this manner, impedance variations can be correlated to mechanical interfacial contact forces exerted by the tissue in contact with the top of the sensor array. However, because of the use of an electrochemical sensing scheme, the sensor is particularly sensitive to changes in electrolyte compared to other membrane-based force sensors. There exists a trade-off between electrolyte sensitivity and mechanical flexibility; current membrane-based force sensors

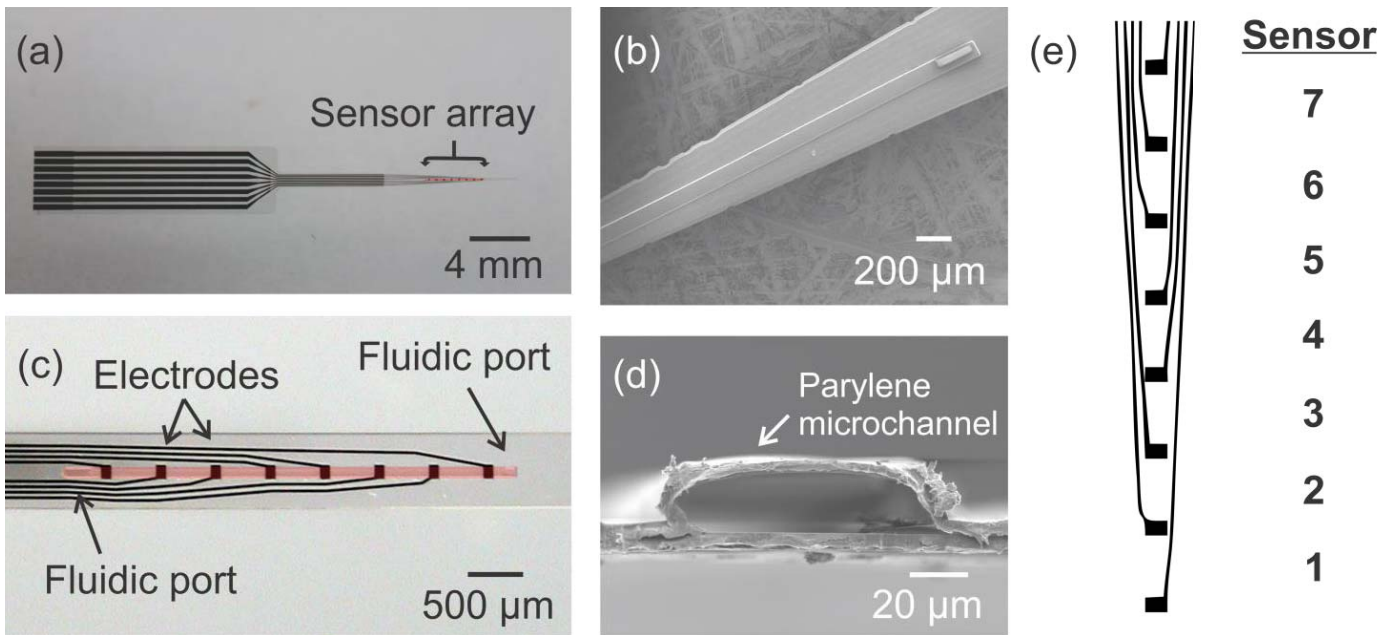


Fig. 3. (a) Optical micrograph of full sensor array and integrated Parylene cable. Microchannel structure is highlighted in pink. (b) Scanning electron micrograph (SEM) image showing top view of the sensor array with a fluidic port at the end of the microchannel. (c) Top-down image of Parylene microchannel (pink) indicating the electrodes and fluidic ports located at the ends. (d) SEM showing the cross section of the  $20\ \mu\text{m}$  Parylene microchannel sensing structure. (e) Microelectrode layout and sensor numbering based on adjacent electrode pairs.

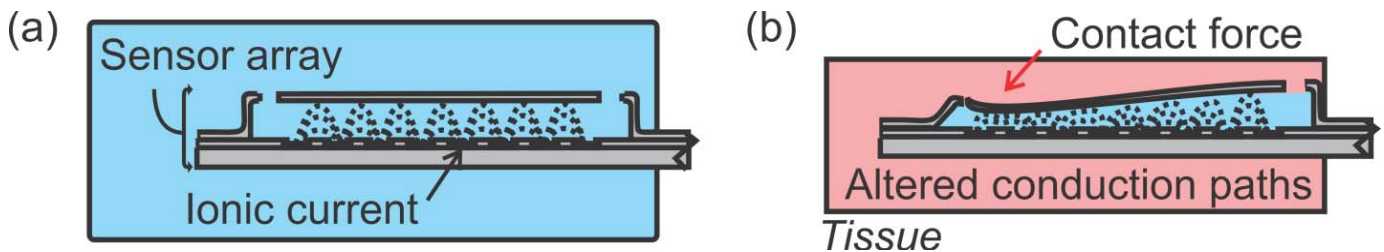


Fig. 4. Operation principle of the Parylene microchannel-based interfacial force sensor (a) pre and (b) post insertion into tissue.

require bulk, hermetic packaging to resist the high saline environment of the body. By leveraging the electrolytic environment for sensing, the EC-MEMS sensor design eliminates the bulky packaging required by current sensors and results in a low-profile and flexible device ideal for a chronic implant.

The intracortical Parylene-based EC-MEMS sensor array technology is based on distributed sensors arranged along a Parylene microchannel-sensing element ( $100\ \mu\text{m} \times 4.5\ \text{mm} \times 24\ \mu\text{m}$ ) to match the footprint of a ceramic-based cortical probe [23], notable for exceptional chronic recording and electrochemical sensing performance within monkey cortical work, for initial testing. The microchannel encloses eight fluidically-coupled platinum (Pt) electrodes ( $100\ \mu\text{m} \times 130\ \mu\text{m}$ ) arranged at a pitch of  $500\ \mu\text{m}$ , with adjacent pairs forming a sensor unit (Fig. 3). Each array consists of seven sensor “pixels” along the length of the probe; sensor 1 begins at the tip of the probe and sensor 7 is at its base (Fig. 3e). This sensor configuration was selected to maximize sensor density over the area of interest defined by the cortical probe layout and to maintain transducer symmetry.

Etched fluidic ports at the channel ends allow the surrounding electrolyte to fill the channel. Fluid can flow freely between the external environment and the channel via these access ports. A Parylene flat flexible cable (FFC) with eight leads was also integrated into the device design in order to establish electrical contact via a zero-insertion-force (ZIF) connector.

Because of the flexible and thin Parylene microchannel structure ( $4\ \mu\text{m}$  thickness), contact forces (i.e. elastic and spring forces) from surrounding cortical tissue will deform the top surface along the length of the probe (Fig. 4). It is important to note here that the sensors are insensitive to hydrostatic forces because the fluidic ports allow for an open fluidic connection between the inside and outside of the channel; the sensing element deforms primarily due to mechanical contact forces on the top channel surface. The seven sensor pixels along this length quantify the distribution of interfacial forces that the probe imparts on the surrounding cortical tissue during insertion, extending a similar concept from previous sensor technology developed to quantify interfacial forces produced during implantation of an epiretinal implant onto the retinal surface [24]. The flexible substrate (total thickness =  $10\ \mu\text{m}$ )

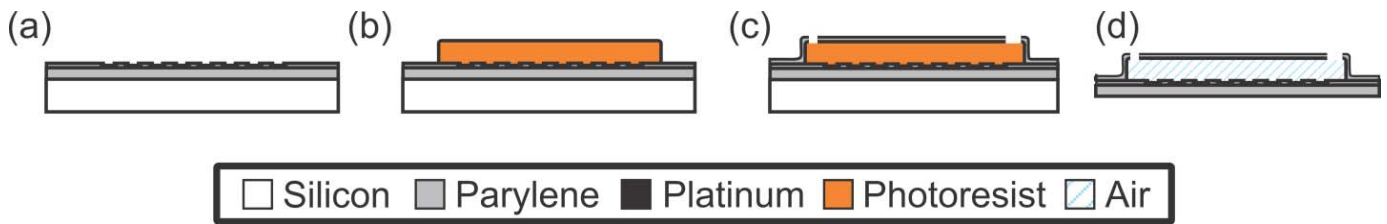


Fig. 5. Overview of fabrication process for the Parylene-based EC-MEMS sensor array. (a) Platinum electrodes and contact pads were patterned by liftoff onto a Parylene substrate; an insulation layer was also deposited and etched to reveal electrode sites. (b) Sacrificial photoresist was spun on and patterned to form the microchannel structure. (c) Another Parylene layer was deposited to form the deformable top membrane structure and fluidic ports were etched into the top using oxygen plasma; the device perimeter was then etched using  $O_2$  plasma. (d) Devices were released off the carrier wafer and soaked in acetone to remove the sacrificial photoresist. Then the devices were filled with  $1\times$  PBS prior to testing.

also allows for simple, low-profile instrumentation of the ceramic cortical probes. The microchannel and electrode layout can be modified to fit probe footprints of a variety of designs, demonstrating its robustness and versatility.

### III. DEVICE FABRICATION AND PACKAGING

Standard surface micromachining processes were used for sensor array fabrication (Fig. 5). All fabrication processes were performed at low temperatures ( $90^\circ\text{C}$ ) to prevent excessive thermal cycling of the Parylene structural material. Parylene was chosen as the sensor material for its biocompatibility, mechanical strength, electrical insulation properties, and compatibility with micromachining processes.

Platinum electrodes and contact pads ( $2000\text{ \AA}$ ) were patterned by lift-off on a Parylene substrate ( $5\text{ }\mu\text{m}$ ) coated onto a silicon carrier wafer. Following deposition of a Parylene insulation layer ( $1.5\text{ }\mu\text{m}$ ), openings for electrodes and contact pads were etched using oxygen plasma. A sacrificial photoresist (PR) process was used to form the microchannel, but because of the relatively tall height ( $20\text{ }\mu\text{m}$ ), two PR layers (AZ 4620; AZ Electronic Materials, Branchburg, NJ) were spun on (each  $10\text{ }\mu\text{m}$  thick) to accurately and uniformly establish the desired microchannel height. Following this, a  $4\text{ }\mu\text{m}$  thick layer of Parylene was deposited to form the final device structure. This thickness was important as it set the sensor mechanics; thicker films would displace less than thinner microchannels. A thickness of  $4\text{ }\mu\text{m}$  was chosen based on previous sensor work on measuring contact forces between epiretinal implants and retinal tissue [14]. Fluidic access ports at the channel ends were opened by oxygen plasma. Finally, to facilitate precise shaping of the array for attachment to a fine ceramic shank tip, arrays were singulated using oxygen plasma.

Devices were released from the wafer by stripping the protective photoresist mask for the cut-out etch with acetone, and then submerging the wafer in DI water. The hydrophobicity of the Parylene polymer allowed the arrays to easily separate from the native oxide of the silicon carrier wafer and lift-off the surface. Sacrificial photoresist within the channel was then removed by immersion in acetone and isopropyl alcohol following rinse in deionized water. The individual arrays were then let to air dry overnight. The mechanical integrity of the Parylene microstructure was sufficient to avoid stiction during the drying process.

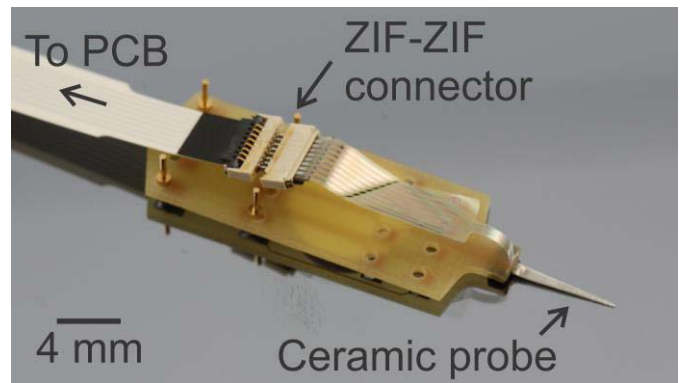


Fig. 6. Image showing integrated Parylene flex cable inserted into a ZIF-ZIF connector for electrical connection to the sensor.

Following fabrication, sensors underwent post-processing steps for electrical packaging to the measurement system. Electrical connections to the integrated Parylene cable was made via an 8 contact ZIF connector (8 channel,  $0.5\text{ mm}$  pitch; Hirose Electric Co., Simi Valley, CA), a hinge-based connector that allows for a zero-insertion force method when the cable is inserted into the bay of the connector. As the connector requires a cable thickness of  $300\text{ }\mu\text{m}$ , a polyetheretherketone (PEEK) polymer backing was applied as a stiffener on the back of the contact pad region. This connection scheme enabled rapid, epoxy-less connections to multiple contact pads supported on our flexible Parylene substrate [25] (Fig. 6).

The ZIF connector used in this packaging method was a ZIF-ZIF adaptor that connected the sensor array to a commercial polymer flexible cable (Molex Inc., Lisle, IL) that was thicker and more robust for handling; the ZIF-ZIF adaptor was made by soldering the legs of two separate ZIF connectors together. The addition of the polymer flexible cable allowed for more robust, repeatable connections into the custom measurement PCB via another ZIF connector compared to the thin Parylene cable.

### IV. EXPERIMENTAL METHODS

To measure the electrochemical impedance from all seven sensors of the array, a custom multiplexer was designed that allowed for user-controlled switching between various pairs of electrodes for impedance measurement using a precision LCR meter (Agilent E4980A; Agilent Technologies, Santa Clara, CA). The multiplexer was controlled digitally



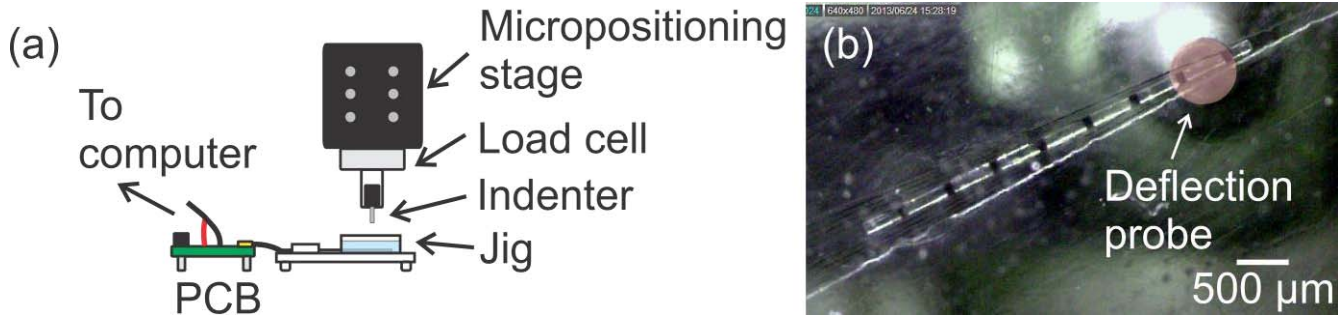


Fig. 7. (a) Load-displacement setup for mechanical and calibration testing of Parylene force sensor array. (b) Optical micrograph taken using a camera underneath testing setup illustrating deflection probe (pink) displacing into sensor element.

through a LabVIEW graphical user interface (GUI) which cycled through adjacent electrode pairs. Impedance was measured at 1 kHz, with an amplitude of 1 V<sub>pp</sub>.

Characterization of the sensors was carried out on the benchtop in a custom acrylic jig designed to keep the sensor array immersed in an electrolyte (1× PBS; Fig. 7a). A flat, circular, probe tip (diameter = 630 μm), attached to a motorized z-axis stage, was used to indent the microchannel in 2 μm increments until reaching the maximum deflection of 20 μm (Fig. 7b). The probe diameter was chosen to cover the entire surface of a sensor unit (60,000 μm<sup>2</sup>). An in-line load cell (0-50 g, LCFA-50; Omega Engineering, Stamford, CT) was used to measure the applied force of the indenting probe during displacement. During this calibration procedure, real-time impedance was measured across all sensor units using LabVIEW software. A 10-minute relaxation step was used between calibrations of sensors to ensure that the microchannel structure returned to the baseline reading (impedance ≤ 0.1% of initial value). Also, to further decouple the sensor units of the array, sensors were calibrated in an order chosen to prevent the sequential testing of two adjacent sensors.

For the case in which these sensors are to be used in chronic implant conditions, additional steps are necessary to counter observed soaking-induced delamination failure of multi-layered Parylene C devices [26]. Thermal annealing of Parylene devices has been reported to improve interlayer adhesion and device lifetime during prolonged soak conditions [27]–[31]. The annealing process is thought to increase polymer chain entanglement between the Parylene layers and provide additional mechanical anchoring between the chains to resist delamination and improve moisture barrier performance [32]. Annealing is achieved at temperatures above the glass transition temperature of Parylene ( $T_g = 60\text{--}90\text{ }^\circ\text{C}$ ) in order to provide enough energy for movement of the polymer chains. However, the heat treatment of Parylene is also known to produce changes in crystallinity of the bulk polymer (hence the importance of Parylene's thermal budget during device fabrication) [33], which may influence device performance. Because of this, device performance pre- and post-annealing was evaluated to assess any mechanical changes due to the annealing process.

Sensor arrays were placed within a vacuum oven (10 mTorr), which was ramped at 1.6 °C/min to 200 °C.

Following a thermal soak time of 48 hours, the devices were cooled overnight (~15 hours) under vacuum, and then removed for post-process characterization. Untreated sensors were released off the wafer and also tested for comparison. As the mechanical and electrochemical properties of the sensor drive its performance, the effects of annealing on these two aspects were analyzed via scanning electron microscopy (SEM), profilometry, and load-deflection tests of the sensing structures immersed in an electrolyte solution (1× PBS). Two point electrochemical impedance spectroscopy (EIS; 1× PBS, 20 Hz–1 MHz), a commonly used electrochemical technique to assess electrode surface properties, was conducted between adjacent electrodes using a Gamry Reference 600 potentiostat (Gamry Instruments, Warminster, PA) to determine changes to the electrochemical properties of the sensing electrodes.

## V. RESULTS AND DISCUSSION

The sensor mechanical and force response was characterized on unannealed devices after the optimal electrochemical impedance measurement frequency was evaluated. The effects of thermal annealing on sensor performance were then evaluated and compared to un-annealed samples. Finally, the sensor array was mounted onto a ceramic cortical probe for benchtop insertion tests to demonstrate proof-of-concept sensor operation.

### A. Obtaining $f_{\text{meas}}$

Prior to calibration, EIS was performed across all sensor electrode pairs to determine the optimal  $f_{\text{meas}}$  at which the solution resistance dominates the complex impedance response. An excitation frequency of ~2 kHz was found to correspond to the maximum resistive response at a phase value near 0° (Fig. 8). However, to ensure signal fidelity from parasitic capacitances of the measurement system, all subsequent impedance measurements were performed at 1 kHz, which was sufficient to isolate the solution resistance.

### B. Sensor Characterization

The Parylene microchannel was found to deform uniformly along the length of the channel, as the displacement per applied force was similar across runs for each sensor (Fig. 9).

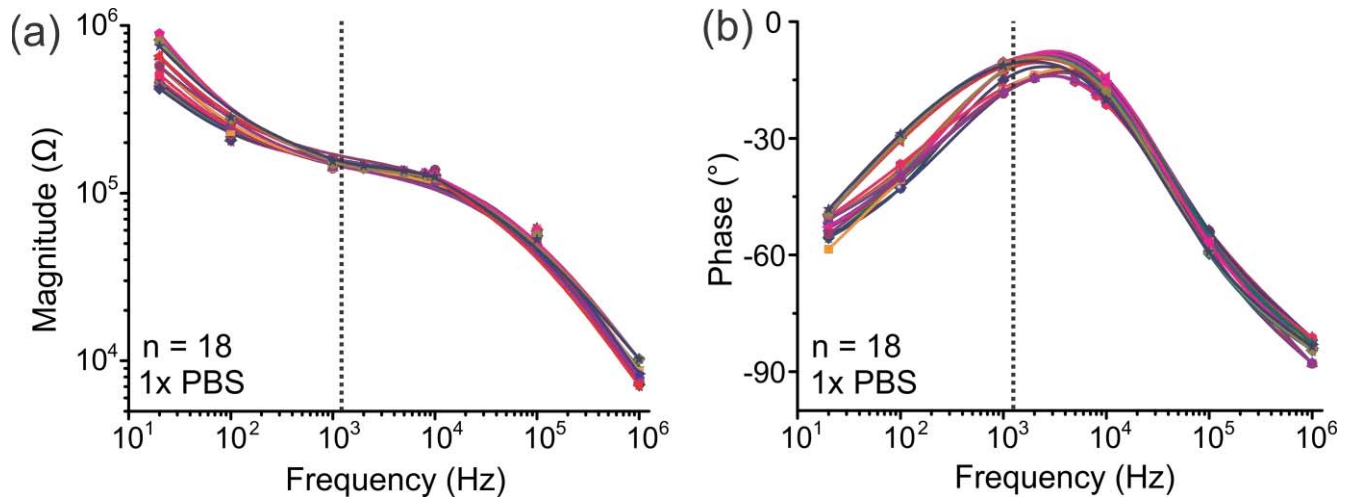


Fig. 8. Impedance (a) magnitude and (b) phase plots of 18 individual sensors. An  $f_{\text{meas}}$  of 1 kHz (dashed line) was selected and corresponds to maximum resistive response at a phase value near  $0^\circ$ .

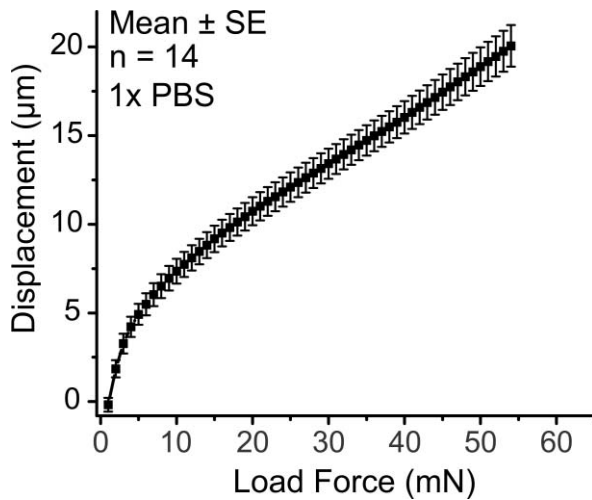


Fig. 9. Load-displacement plot for the Parylene microchannel sensing element of the EC-MEMS sensor array indicating that operational uniformity was maintained despite their differing locations along the fluidically coupled channel.

Plotting cyclic loading/unloading force-displacement data generated curves that capture the sensor's dynamic mechanical behavior. The channel structures were deformed at a rate of  $1 \mu\text{m/s}$ , held at a maximum deflection of  $20 \mu\text{m}$  for 20 s and then returned to the initial position at  $1 \mu\text{m/s}$ ; the next loading cycle was initiated 30 s following the return to resting position. Five consecutive loading/unloading cycles were applied. Results indicated negligible hysteresis regardless of the sensor position (Fig. 10). Although higher frequency dynamic analysis was not performed, the frequency response of the Parylene microchannel structure in air was calculated to be 570 kHz using FEM software (COMSOL, Burlington, MA). It is expected that this frequency would be further reduced to account for fluidic damping to a conservative estimate of 10-100 Hz, as observed in other resonant frequency studies of Parylene thin film diaphragms [14], [34]. Fortunately, as the interfacial force dynamics within the cortex are very slow

(maximum  $\sim 3\text{--}5$  Hz of micromotion due to vascular pulsing [5]), the current sensor design is more than sufficient for this application. Additional dynamic loading tests were also performed to assess the effects of varying step-sizes (4, 6, 12,  $20 \mu\text{m}$ ) on possible deflection-linked dynamic mechanical responses. Results indicated reproducible and repeatable displacement-load force curves for varying displacements and small hysteresis over five cycles (0.01 Hz) at each depth. In some instances however, considerable hysteresis was observed, which suggests yield and process variations that can create non-uniform microchannel structures and thus varying mechanical responses (data not shown).

A sensitivity of  $0.13 \pm 0.01$  percentage change in impedance/ $\mu\text{N}$  ( $\%/\mu\text{N}$ ; mean  $\pm$  SE,  $n = 6$ ) was found for each sensor unit (Fig. 11) from the calibration curve, within a sensor working range of 0-60 mN. Without utilizing any signal conditioning techniques, the resolution of the sensor is dependent on the accuracy of the impedance measuring device. Using the high precision LCR meter ("short" measurement function,  $\pm \sim 0.2\%$  impedance magnitude), the resolution of the measurement systems was calculated to be  $\sim \pm 1$  mN.

Mechanical crosstalk was also assessed by indenting a single sensor and monitoring the responses of the other sensors in the array concurrently (Table I). Crosstalk was calculated as the ratio of the percentage change in impedance of the site recorded to that of the site indented. The colored table facilitates visualization of relative crosstalk magnitudes. As indicated in the table below, mechanical crosstalk between sensors was generally  $\sim 2\text{--}10\%$ , allowing for independent discrimination of forces based on location along the length of the sensor array.

### C. Annealing Effects on Sensor Performance

Detailed results and analysis of the effects of thermal annealing on sensor performance can be found in previous work [35], but key points are briefly mentioned here for completeness. Load-deflection tests revealed a  $\sim 1.6\times$  increase in the stiffness of the structure following annealing,

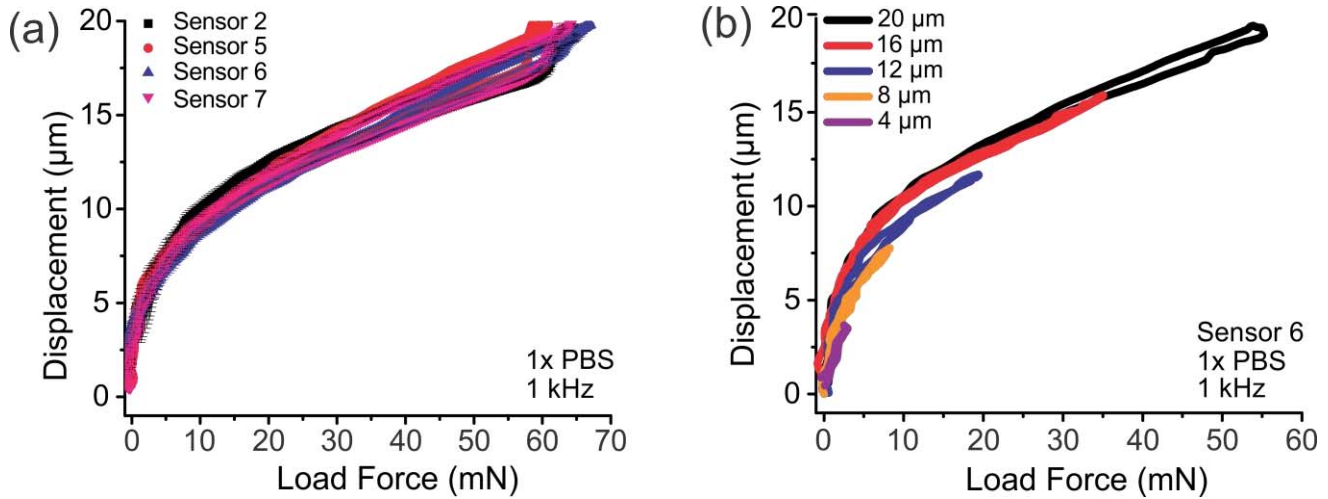


Fig. 10. Loading and unloading cycle results of (a) four different sensors at maximum deflection and (b) at various deflection depths indicating negligible hysteresis.

TABLE I

CROSSTALK WAS CALCULATED AS THE RATIO OF THE PERCENT IMPEDANCE CHANGE OF THE SITE RECORDED OVER THAT OF THE SITE INDENTED. MEAN  $\pm$  SE,  $n = 3$ . \* FOR ROWS 1 AND 4,  $n = 2$

		Site Recorded						
		1	2	3	4	5	6	7
Site Indented	1*	1.00 $\pm$ 0.00	0.03 $\pm$ 0.01	0.02 $\pm$ 0.01	-0.02 $\pm$ 0.03	-0.01 $\pm$ 0.02	-0.01 $\pm$ 0.03	-0.01 $\pm$ 0.01
	2	0.28 $\pm$ 0.27	1.00 $\pm$ 0.00	-0.03 $\pm$ 0.03	-0.04 $\pm$ 0.03	-0.02 $\pm$ 0.02	-0.13 $\pm$ 0.12	-0.19 $\pm$ 0.13
	3	-0.14 $\pm$ 0.10	0.05 $\pm$ 0.20	1.00 $\pm$ 0.00	-0.06 $\pm$ 0.07	-0.05 $\pm$ 0.05	-0.07 $\pm$ 0.08	-0.05 $\pm$ 0.05
	4*	0.03 $\pm$ 0.02	-0.25 $\pm$ 0.27	0.08 $\pm$ 0.21	1.00 $\pm$ 0.00	0.09 $\pm$ 0.04	0.07 $\pm$ 0.04	0.08 $\pm$ 0.03
	5	-0.03 $\pm$ 0.02	-0.03 $\pm$ 0.03	-0.01 $\pm$ 0.01	0.05 $\pm$ 0.02	1.00 $\pm$ 0.00	0.02 $\pm$ 0.02	0.01 $\pm$ 0.01
	6	-0.01 $\pm$ 0.01	-0.01 $\pm$ 0.02	0.02 $\pm$ 0.01	-0.01 $\pm$ 0.02	-0.07 $\pm$ 0.14	1.00 $\pm$ 0.00	0.05 $\pm$ 0.02
	7	-0.02 $\pm$ 0.00	0.01 $\pm$ 0.01	-0.01 $\pm$ 0.01	0.03 $\pm$ 0.03	0.02 $\pm$ 0.02	0.12 $\pm$ 0.02	1.00 $\pm$ 0.00

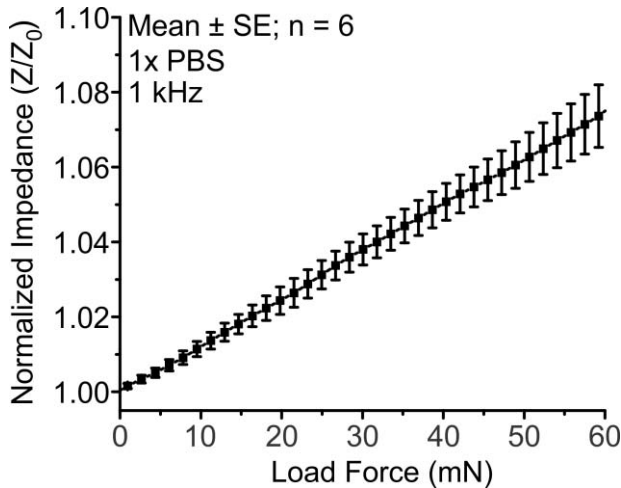


Fig. 11. Obtained calibration curve for the EC-MEMS sensor showing linearity within the force range of 0-60 mN.

likely due to a combination of microchannel height shrinkage and an increase in the elastic modulus of the annealed Parylene attributable to increased polymer crystallinity [36]. EIS results indicated a decrease in the surface roughness of the electrodes following annealing, due to smoothing of the

thin-film metal and underlying Parylene [37]. These changes decreased the sensitivity of the sensor by 24%. FEM utilizing COMSOL to model the observed changes following annealing (i.e. increased Parylene stiffness and decrease in electroactive surface area) suggested that the increase in stiffness of the Parylene film contributed the most to the differences in sensor performance for these devices. As the sensing mechanism is chiefly derived from the mechanics of the sensing structure, any changes to the stiffness of the polymer have a significant impact on sensor response.

#### D. Instrumentation of Cortical Probes

Instrumentation of a representative neural probe, an inert ceramic cortical probe [38] notable for exceptional chronic recording and electrochemical sensing performance within monkey cortical work, was achieved (Fig. 12). To ensure that the recording and sensing capabilities of the ceramic probe were not lost, the sensor arrays were attached to the back-side (non-electrode-side) of the probes using a thin layer of biocompatible super glue (Adhesive Systems MG 100 USP Class VI; Adhesive Systems, Inc., Frankfort, IL). The sensor array was manually aligned and adhered to the ceramic probe. Handling tabs designed into

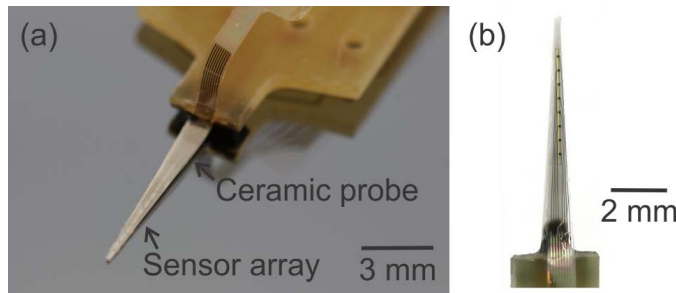


Fig. 12. (a) Image of the ceramic cortical shank instrumented with fully packaged sensor array. (b) Optical micrograph of probe surface illustrating the electrodes of the sensor array. Microchannel sensing element has been highlighted yellow.

the array allowed for precise manual placement. For benchtop testing, instrumented ceramic probes were mounted to a custom acrylic jig which allowed integration with an automated probe insertion setup.

#### E. Benchtop Insertion Experiments

The cortical sensor array was demonstrated on benchtop by replicating an implantation via probe insertion into 0.5% agarose, a commonly used model for cortical tissue [39], [40], immersed in a 1× phosphate buffered saline (PBS) solution to mimic *in vivo* conditions. Sensor arrays were filled via immersion with 1× PBS electrolyte following a short immersion in isopropyl alcohol (a Parylene wetting step to facilitate diffusion of the polar PBS into the microchannel). Instrumented ceramic probes were then inserted to a depth of 3.5 mm into agarose at three different speeds: 0.01 mm/s (slow), 0.03 mm/s (medium), and 0.1 mm/s (fast), held at the maximum displacement for five minutes, and extracted at the same speed while sensor array impedances were measured in real time. Impedance was measured by a LabVIEW-interfaced precision LCR meter (1 V<sub>pp</sub> sinusoid, 1 kHz) via a multiplexing PCB for multi-channel impedance measurement across the seven sensors of the array.

An external 50 g load cell was used for measurement of normal forces generated during insertion. The probe and load cell were affixed to a motorized micropositioning stage that controlled insertion speed and depth into the tissue phantom (Fig. 13a). The motorized stage, LCR meter, and PCB digital switching all interfaced with LabVIEW to give the user control of insertion speed and depth as well as a real-time image (graphical) of the impedance changes (interfacial forces) across the ceramic probe (Fig. 13b).

Two insertion experiments were performed. In both insertion experiments, some of the observed normalized impedance values (and thus forces) greatly exceeded the calibrated linear range of the sensor. Possible sources for the observed are: (1) observing force ranges much higher than expected and (2) differing displacement profiles (i.e. non-normal to top surface) of the sensor from what was characterized. Slight changes in electrolyte conductivity from agarose gel filling into the channel through the fluidic ports during insertion may occur, but may be unlikely as diffusion from a gel into solution would occur at a longer time scale than mechanical

deformation during insertion at these speeds. Despite this however, the percentage change in impedance data suggests a trend in interfacial pressures experienced as a function of insertion speed.

Noting that sensors 1-7 begin at the shank tip and move to its base, data indicated that a majority of the interfacial forces during insertion are within the first millimeter of the electrode shank (the first sensor). This is also evidenced by the results across all three insertion speeds; the maximum percentage change in impedance of the first sensor is considerably higher than that of the remaining sensors higher up on the shank (Table II). We attribute the interfacial forces experienced at the tip during insertion to the tissue displacement and propagation of the electrode shank track generated by the probe. Additional force is imposed by tissue as it is being displaced during insertion.

By varying insertion speed, we observed that interfacial forces at the shank tip (first millimeter) decrease as the speed increases. Slower insertion speeds allow for a longer travel time through tissue, increasing shank-tissue adhesion and thus the frictional forces between the shank and tissue. Results confirm that faster speeds decrease the interfacial forces experienced at the tip (by tissue displacement and frictional forces) [1] as the maximum impedance change is lower by nearly 60%.

This effect of speed on interfacial forces is consistent throughout the length of the shank. At the slowest speed, increased frictional forces resulting in additional array deformation during insertion give rise to higher average impedance change in other sensors; Sensors 2-7 recorded an average maximum impedance change of 12% compared to 2% and 1% at the medium and fast speeds, respectively. Therefore, faster speeds also reduce adhesion forces between the shank and surrounding tissue along the length of the tip.

#### VI. INSERTION MECHANICS CONSIDERATIONS

Benchtop insertion data indicated that interfacial forces were concentrated at the tip. As these interfacial forces are a result of tissue strain during insertion, we would expect to find a similar trend *in vivo* with high tissue strains localized at the tip. This is supported by modeling [8], [10] and *in vitro* [13] efforts that assess tissue strains during the insertion of stiff probes. The probe track is often compared to a mode I, or opening mode, of a crack, which produces a triangular profile that lends to higher interfacial forces at the tip. These results are further confirmed by an *ex vivo* study by Bjornsson *et al* [11], where probe insertions established twice the tissue strain at the tip compared to the base of the probe. Even within *in vivo* experiments [41], [42], increased glial response and reduced neuronal presence was observed at the tip of the probe, most likely due to the relatively high forces and tissues strains that can cause additional damage. Our work and those in literature suggest that probe designs should have electrodes concentrated away from the tip to minimize recording zones within these highly damaged regions.

In addition to probe design, another important factor that influences tissue damage is the speed of insertion. The precise



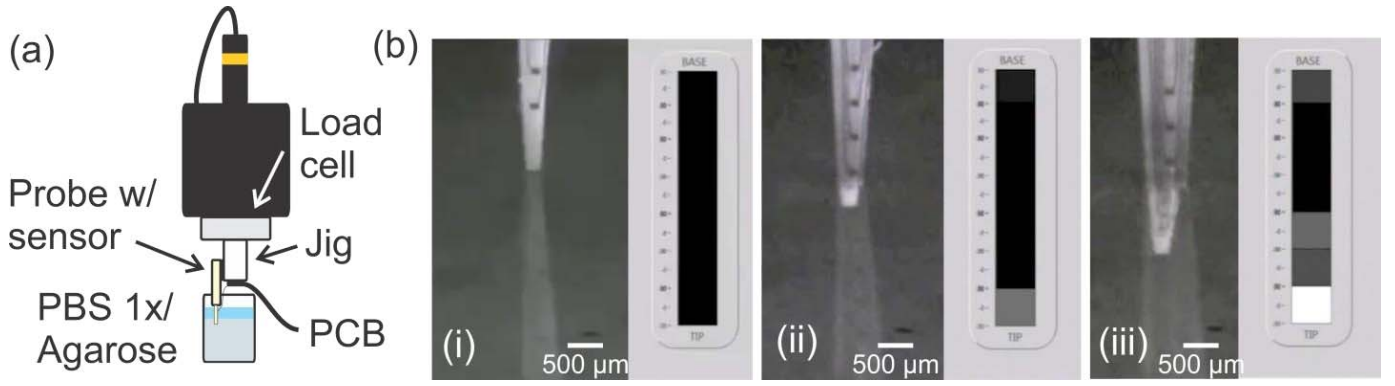


Fig. 13. (a) Schematic of benchtop insertion testing setup. (b) Screenshot image of user GUI during benchtop testing: (Left) a video stream of the insertion process using a USB microscope. (Right) heat map of GUI to show the distribution of force magnitudes along the length of the probe. Images illustrate the progression of the instrumented probe from (i) before insertion, (ii) only tip inserted, (iii) half of probe inserted.

TABLE II

TABLE OF OBSERVED DISTRIBUTIONS OF IMPEDANCES ALONG THE LENGTH OF THE PROBE FOR TWO DIFFERENT INSERTION EXPERIMENTS

Experiment #	Insertion speed (mm/s)	Max. impedance change: Sensor 1 (shank tip)	Avg. max. impedance change: Sensors 2-7 (n=6, Mean $\pm$ SE)
1	0.01	102 %	20 $\pm$ 1.9 %
	0.03	70 %	7 $\pm$ 0.8 %
	0.1	26 %	4 $\pm$ 0.4 %
2	0.01	87 %	12 $\pm$ 3 %
	0.03	38 %	2 $\pm$ 1 %
	0.1	28 %	1 $\pm$ 0.6 %

effect of speed on tissue damage is still debated, but in general, slower speeds can drag and compress the surrounding tissue and create a path of damage that can extend the kill zone of the implant beyond the probe track as far as 300  $\mu\text{m}$  away [11], [42]. Faster insertion speeds can reduce tissue damage by swiftly transecting the tissue and vasculature during implantation, which cause significantly less tissue compression [42], [43]. In comparing insertion speeds, our results indicated that faster speeds produced smaller interfacial forces, which suggests smaller tissue strains (and thus damage) during insertion. This result is further supported by *ex vivo* insertion mechanics studies where faster insertion rates ( $\sim 2$  mm/s) were found to decrease microvasculature damage and tissue strain compared to slower speeds (125-500  $\mu\text{m/s}$ ) [11]. Unfortunately, tissue responses to insertion speeds of 125 and 500  $\mu\text{m/s}$  [11] and 10 and 100  $\mu\text{m/s}$  [42] were found to be similar, suggesting that insertion mechanics are comparable within the range of 10-500  $\mu\text{m/s}$  for probes with cross sectional dimensions of  $\sim 100 \times 100$   $\mu\text{m}$ . Probes with larger dimensions (e.g.  $\sim 1$  mm in diameter for deep-brain stimulation electrodes) might observe greater differences between speeds.

Insertion speeds greater than 2 mm/s have been known to compensate for blunt probe design, as observed in a speed of 8.3 m/s used to pneumatically implant the three-dimensional, 100 site Utah electrode array to avoid elastic compression of the cortical surface [44]. On the other side of the spectrum, some efforts target very slow speeds, on the range of neuronal or microglial movement (0.42  $\mu\text{m/s}$ ), to displace cells and vasculature without

tearing them, and have also demonstrated improved tissue immune response [45]. Overall these results suggest that speeds (whether extremely fast or slow) are chosen based on the probe structure and design to minimize tissue damage, and should be considered on an individual probe to probe basis. It is the hope that additional experiments with this technology, in combination with histological data and *in vivo* neurophysiological measurements, can help to clarify or confirm some of these debated topics to realize the promise of neural prosthetics.

## VII. CONCLUSION

EC-MEMS sensors are straightforward to fabricate and implement. Here, we have demonstrated the design, fabrication, characterization, and benchtop implementation of a Parylene-based force sensor array for studying mechanical interactions in neural probes. We demonstrated that annealing introduces both mechanical and electrochemical changes that effect sensor performance. We have also presented a method to attach these thin, low-profile sensors to ceramic cortical probes and quantitative data on interfacial forces in model experiments involving insertion speed. Previous work using these sensors also validated their capability on measuring micromotion events in gel phantom models [23]. Force ranges and sensitivity for a particular EC-MEMS force sensor can also be tuned by changes in device geometry and thickness to accommodate interfacial force ranges expected during insertion. The ease of fabrication, simple wet transduction mechanism, and low-profile integration opens possibilities for use of this technology in a variety of *in vivo* applications.

Specifically in looking at insertion mechanics, an analysis limited to normal insertion forces might suggest that slower insertion speeds benefit insertion by decreasing the forces encountered during probe implantation. However, it is also important to consider the contribution of interfacial forces prior to reaching a conclusion on insertion parameters. Faster insertion speeds not only reduce the forces at the shank tip created during insertion, but also the frictional forces and thus tissue strains observed. Measurement of interfacial forces elucidates the locations and magnitudes of tissue displacement and frictional forces during insertion. Instrumentation of different neural interfaces with sensors such as these can aid in the further development of more reliable chronic neural prosthetics as enabling devices.

#### ACKNOWLEDGMENT

The authors would like to acknowledge Mr. E. Peter Washabaugh VI, Mr. Louis Jug, and Ms. Alejandra Gonzales Calle, for invaluable assistance with device characterization. We would also like to thank Dr. Greg Gerhardt of the University of Kentucky for providing the ceramic cortical probes, and Dr. Donghai Zhu and the members of the USC Biomedical Microsystems Laboratory for their assistance.

#### REFERENCES

- [1] V. S. Polikov, P. A. Tresco, and W. M. Reichert, "Response of brain tissue to chronically implanted neural electrodes," *J. Neurosci. Methods*, vol. 148, no. 1, pp. 1–18, 2005.
- [2] K. A. Potter, A. C. Buck, W. K. Self, and J. R. Capadona, "Stab injury and device implantation within the brain results in inversely multiphasic neuroinflammatory and neurodegenerative responses," *J. Neural Eng.*, vol. 9, no. 4, p. 046020, 2012.
- [3] A. Gilletti and J. Muthuswamy, "Brain micromotion around implants in the rodent somatosensory cortex," *J. Neural Eng.*, vol. 3, no. 3, pp. 189–195, Sep. 2006.
- [4] N. H. Hosseini, R. Hoffmann, S. Kisban, T. Stieglitz, O. Paul, and P. Ruther, "Comparative study on the insertion behavior of cerebral microprobes," in *Proc. 29th Annu. Int. Conf. IEEE Eng. Med. Biol. Soc. (EMBS)*, Aug. 2007, pp. 4711–4714.
- [5] R. Das, D. Gandhi, S. Krishnan, L. Saggere, and P. J. Rousche, "A benchtop system to assess cortical neural interface micromechanics," *IEEE Trans. Biomed. Eng.*, vol. 54, no. 6, pp. 1089–1096, Jun. 2007.
- [6] C. Tian and J. He, "Monitoring insertion force and electrode impedance during implantation of microwire electrodes," in *Proc. 27th Annu. Int. Conf. Eng. Med. Biol. Soc. (IEEE-EMBS)*, Jan. 2005, pp. 7333–7336.
- [7] D. H. Szarowski *et al.*, "Brain responses to micro-machined silicon devices," *Brain Res.*, vol. 983, nos. 1–2, pp. 23–35, Sep. 2003.
- [8] S. P. DiMaio and S. E. Salcudean, "Needle insertion modeling and simulation," *IEEE Trans. Robot. Autom.*, vol. 19, no. 5, pp. 864–875, Oct. 2003.
- [9] H. Lee, R. V. Bellamkonda, W. Sun, and M. E. Levenston, "Biomechanical analysis of silicon microelectrode-induced strain in the brain," *J. Neural Eng.*, vol. 2, no. 4, p. 81, 2005.
- [10] J. Subbaroyan, D. C. Martin, and D. R. Kipke, "A finite-element model of the mechanical effects of implantable microelectrodes in the cerebral cortex," *J. Neural Eng.*, vol. 2, no. 4, p. 103, 2005.
- [11] C. S. Bjornsson *et al.*, "Effects of insertion conditions on tissue strain and vascular damage during neuroprosthetic device insertion," *J. Neural Eng.*, vol. 3, no. 3, p. 196, 2006.
- [12] K. Seidl, B. Lemke, H. Ramirez, S. Herwik, P. Ruther, and O. Paul, "CMOS-based high-density silicon microprobe for stress mapping in intracortical applications," in *Proc. IEEE 23rd Int. Conf. Micro Electro Mech. Syst. (MEMS)*, Jan. 2010, pp. 35–38.
- [13] A. A. Sharp, A. M. Ortega, D. Restrepo, D. Curran-Everett, and K. Gall, "In vivo penetration mechanics and mechanical properties of mouse brain tissue at micrometer scales," *IEEE Trans. Biomed. Eng.*, vol. 56, no. 1, pp. 45–53, Jan. 2009.
- [14] C. A. Gutierrez and E. Meng, "Impedance-based force transduction within fluid-filled Parylene microstructures," *J. Microelectromech. Syst.*, vol. 20, no. 5, pp. 1098–1108, Oct. 2011.
- [15] C. A. Gutierrez, C. McCarty, B. Kim, M. Pahwa, and E. Meng, "An implantable all-Parylene liquid-impedance based MEMS force sensor," in *Proc. IEEE 23rd Int. Conf. Micro Electro Mech. Syst. (MEMS)*, Jan. 2010, pp. 600–603.
- [16] C. A. Gutierrez and E. Meng, "A dual function Parylene-based biomimetic tactile sensor and actuator for next generation mechanically responsive microelectrode arrays," in *Proc. Int. Conf. TRANSDUCERS*, Denver, CO, USA, Jun. 2009, pp. 2194–2197.
- [17] R. Sheybani, N. E. Cabrera-Munoz, T. Sanchez, and E. Meng, "Design, fabrication, and characterization of an electrochemically-based dose tracking system for closed-loop drug delivery," in *Proc. Annu. Int. Conf. IEEE Eng. Med. Biol. Soc. (EMBS)*, Aug./Sep. 2012, pp. 519–522.
- [18] L. Yu and E. Meng, "A microbubble pressure transducer with bubble nucleation core," in *Proc. IEEE 27th Int. Conf. Micro Electro Mech. Syst. (MEMS)*, San Francisco, CA, USA, Jan. 2014, pp. 104–107.
- [19] J. E. B. Randles, "Kinetics of rapid electrode reactions," *Discussions Faraday Soc.*, vol. 1, pp. 11–19, Mar. 1947.
- [20] H. Helmholtz, "Studien über electrische Grenzschichten," *Ann. Phys.*, vol. 243, no. 7, pp. 337–382, 1879.
- [21] D. A. Robinson, "The electrical properties of metal microelectrodes," *Proc. IEEE*, vol. 56, no. 6, pp. 1065–1071, Jun. 1968.
- [22] D. R. Merrill, M. Bikson, and J. G. R. Jefferys, "Electrical stimulation of excitable tissue: Design of efficacious and safe protocols," *J. Neurosci. Methods*, vol. 141, no. 2, pp. 171–198, 2005.
- [23] B. J. Kim, C. A. Gutierrez, G. A. Gerhardt, and E. Meng, "Parylene-based electrochemical-MEMS force sensor array for assessing neural probe insertion mechanics," in *Proc. IEEE 25th Int. Conf. Micro Electro Mech. Syst. (MEMS)*, Jan./Feb. 2012, pp. 124–127.
- [24] C. A. Gutierrez, "Development of flexible polymer-based MEMS technologies for integrated mechanical sensing in neuroprosthetic systems," Ph.D. dissertation, Dept. Biomed. Eng., Univ. Southern California, Los Angeles, CA, USA, 2011.
- [25] C. A. Gutierrez, C. Lee, B. Kim, and E. Meng, "Epoxy-less packaging methods for electrical contact to Parylene-based flat flexible cables," in *Proc. 16th Int. Solid-State Sens., Actuators, Microsyst. Conf. (TRANSDUCERS)*, Jun. 2011, pp. 2299–2302.
- [26] J. H. Chang, B. Lu, and Y.-C. Tai, "Adhesion-enhancing surface treatments for Parylene deposition," in *Proc. 16th Int. Solid-State Sens., Actuators, Microsyst. Conf. (TRANSDUCERS)*, Jun. 2011, pp. 390–393.
- [27] C. Hassler, R. P. von Metzen, P. Ruther, and T. Stieglitz, "Characterization of Parylene C as an encapsulation material for implanted neural prostheses," *J. Biomed. Mater. Res. B, Appl. Biomater.*, vol. 93B, no. 1, pp. 266–274, 2010.
- [28] J.-M. Hsu, L. Rieth, R. A. Normann, P. Tathireddy, and F. Solzbacher, "Encapsulation of an integrated neural interface device with Parylene C," *IEEE Trans. Biomed. Eng.*, vol. 56, no. 1, pp. 23–29, Jan. 2009.
- [29] W. Li, D. Rodger, P. Menon, and Y.-C. Tai, "Corrosion behavior of Parylene-metal-Parylene thin films in saline," *ECS Trans.*, vol. 11, no. 18, pp. 1–6, Oct. 2008.
- [30] W. Li, D. C. Rodger, E. Meng, J. D. Weiland, M. S. Humayun, and Y.-C. Tai, "Flexible Parylene packaged intraocular coil for retinal prostheses," in *Proc. Int. Conf. Microtechnol. Med. Biol.*, May 2006, pp. 105–108.
- [31] J. P. Seymour, Y. M. Elkasabi, H.-Y. Chen, J. Lahann, and D. R. Kipke, "The insulation performance of reactive Parylene films in implantable electronic devices," *Biomaterials*, vol. 30, no. 31, pp. 6158–6167, 2009.
- [32] D. C. Rodger *et al.*, "Flexible Parylene-based multielectrode array technology for high-density neural stimulation and recording," *Sens. Actuators B, Chem.*, vol. 132, no. 2, pp. 449–460, 2008.
- [33] J.-M. Hsu, L. Rieth, S. Kammer, M. Orthner, and F. Solzbacher, "Effect of thermal and deposition processes on surface morphology, crystallinity, and adhesion of Parylene-C," *Sensors Mater.*, vol. 20, no. 2, pp. 87–102, 2008.
- [34] J.-M. Wang *et al.*, "Design and fabrication of a diaphragm type thermo-buckled microactuators," in *Proc. 1st IEEE Int. Conf. Nano/Micro Eng. Molecular Syst. (NEMS)*, Jan. 2006, pp. 873–876.
- [35] B. J. Kim, E. P. Washabaugh, and E. Meng, "Annealing effects on flexible multi-layered Parylene-based sensors," in *Proc. IEEE 27th Int. Conf. Micro Electro Mech. Syst. (MEMS)*, Jan. 2014, pp. 825–828.
- [36] R. P. von Metzen and T. Stieglitz, "The effects of annealing on mechanical, chemical, and physical properties and structural stability of Parylene C," *Biomed. Microdevices*, vol. 15, no. 5, pp. 1–9, Oct. 2013.

- [37] M. Grosser and U. Schmid, "The impact of annealing temperature and time on the electrical performance of Ti/Pt thin films," *Appl. Surf. Sci.*, vol. 256, no. 14, pp. 4564–4569, 2010.
- [38] J. J. Burmeister, K. Moxon, and G. A. Gerhardt, "Ceramic-based multisite microelectrodes for electrochemical recordings," *Anal. Chem.*, vol. 72, no. 1, pp. 187–192, Jan. 2000.
- [39] Z.-J. Chen *et al.*, "A realistic brain tissue phantom for intraparenchymal infusion studies," *J. Neurosurgery*, vol. 101, no. 2, pp. 314–322, Aug. 2004.
- [40] F. Pervin and W. W. Chen, "Mechanically similar gel simulants for brain tissues," in *Proc. SEM Annu. Conf.*, Indianapolis, IN, USA, 2010, pp. 9–13.
- [41] A. C. Hoogerwerf and K. D. Wise, "A three-dimensional microelectrode array for chronic neural recording," *IEEE Trans. Biomed. Eng.*, vol. 41, no. 12, pp. 1136–1146, Dec. 1994.
- [42] M. Welkenhuysen, A. Andrei, L. Ameye, W. Eberle, and B. Nuttin, "Effect of insertion speed on tissue response and insertion mechanics of a chronically implanted silicon-based neural probe," *IEEE Trans. Biomed. Eng.*, vol. 58, no. 11, pp. 3250–3259, Nov. 2011.
- [43] D. J. Edell, V. V. Toi, V. M. McNeil, and L. D. Clark, "Factors influencing the biocompatibility of insertable silicon microshafts in cerebral cortex," *IEEE Trans. Biomed. Eng.*, vol. 39, no. 6, pp. 635–643, Jun. 1992.
- [44] P. J. Rousche and R. A. Normann, "A method for pneumatically inserting an array of penetrating electrodes into cortical tissue," *Ann. Biomed. Eng.*, vol. 20, no. 4, pp. 413–422, Jul. 1992.
- [45] A. A. Sharp *et al.*, "Toward a self-deploying shape memory polymer neuronal electrode," *J. Neural Eng.*, vol. 3, no. 4, p. L23, 2006.



**Brian J. Kim** received the B.S. degree in biomedical engineering and mathematics from Duke University, Durham, and the M.S. degree in biomedical engineering from the University of Southern California, Los Angeles, in 2010 and 2013, respectively, where he is currently pursuing the Ph.D. degree in biomedical engineering (Provost's Ph.D. Fellow) with the Biomedical Microsystems Laboratory. His research interests are in the development of Parylene-based microelectromechanical systems devices for intracortical applications, specifically on implantable Parylene-based sensor systems. He was a recipient of the Howard G. Clark Award for Independent Research from Duke University, the Viterbi School of Engineering Early Ph.D. Fellowship, and the University of Southern California Provost's Ph.D. Fellowship.



**Christian A. Gutierrez** received the B.S. degrees in electrical engineering, and business economics and management, in 2005; the M.S. degree in electrical engineering from the California Institute of Technology (Caltech), Pasadena, in 2006; and the Ph.D. degree in biomedical engineering from the University of Southern California (USC), Los Angeles, in 2011. He conducted research with the National Science Foundation's Biomimetic Microelectronic Systems Engineering Research Center and the USC's Biomedical Microsystems Laboratory toward the development of novel impedance-based micro and nanotechnologies for biomedical applications, and focused specifically on the development of retinal prosthesis technologies to restore sight to the blind. While with the Micromachining Laboratory, Caltech, he worked on identifying, analyzing, and implementing power harvesting and storage circuitry for microelectromechanical systems-based power harvesting devices. He is the Co-Founder and Chief Technology Officer of Fluid Synchrony, LLC, where he develops high-performance implantable micropump technology for drug delivery applications. He was a recipient of the Caltech Presidential Scholarship, the Bill and Melinda Gates Millennium Fellowship, and the USC Viterbi School of Engineering Kunzel Fellowship.



**Ellis Meng** (M'02–SM'09) received the B.S. degree in engineering and applied science, and the M.S. and Ph.D. degrees in electrical engineering from the California Institute of Technology (Caltech), Pasadena, in 1997, 1998, and 2003, respectively. She held the Viterbi Early Career Chair with the Viterbi School of Engineering. She has been a Professor with the Department of Biomedical Engineering, University of Southern California, Los Angeles, since 2004. She currently holds a joint appointment with the Ming Hsieh Department of Electrical Engineering. Her research interests include bioMEMS, implantable biomedical microdevices, microfluidics, multimodality integrated microsystems, and packaging. She is a Member of Tau Beta Pi, the Biomedical Engineering Society, the Society of Women Engineers, and the American Society for Engineering Education. She was a recipient of the Intel Women in Science and Engineering Scholarship, the Caltech Alumni Association Donald S. Clark Award, and the Caltech Special Institute Fellowship. She has received the NSF CAREER and the Wallace H. Coulter Foundation Early Career Translational Research Awards. In 2009, she was recognized as one of the TR35 Technology Review Young Innovators under 35.